

1 **LEAST-SQUARES RELU NEURAL NETWORK (LSNN) METHOD**
2 **FOR SCALAR NONLINEAR HYPERBOLIC CONSERVATION LAW***

3 ZHIQIANG CAI[†], JINGSHUANG CHEN[†], AND MIN LIU[‡]

4 **Abstract.** In [6], we introduced the least-squares ReLU neural network (LSNN) method for solving the
5 linear advection-reaction problem with discontinuous solution and showed that the method outperforms mesh-
6 based numerical methods in terms of the number of degrees of freedom. This paper studies the LSNN method
7 for scalar nonlinear hyperbolic conservation law. The method is a discretization of an equivalent least-squares
8 (LS) formulation in the set of neural network functions with the ReLU activation function. Evaluation of the
9 LS functional is done by using numerical integration and conservative finite volume scheme. Numerical results of
10 some test problems show that the method is capable of approximating the discontinuous interface of the underlying
11 problem automatically through the *free* breaking lines of the ReLU neural network. Moreover, the method does not
12 exhibit the common Gibbs phenomena along the discontinuous interface.

13 **Key words.** Least-Squares Method, ReLU Neural Network, Scalar Nonlinear Hyperbolic Conservation Law

14 **AMS subject classifications.**

15 **1. Introduction.** Let Ω be a bounded domain in \mathbb{R}^d ($d = 1, 2$, or 3) with Lipschitz boundary,
16 consider the scalar nonlinear hyperbolic conservation law

17 (1.1)
$$\begin{cases} u_t(\mathbf{x}, t) + \nabla_{\mathbf{x}} \cdot \mathbf{f}(u) = 0, & \text{in } \Omega \times I, \\ u = g, & \text{on } \Gamma_-, \\ u(\mathbf{x}, 0) = u_0(\mathbf{x}), & \text{in } \Omega, \end{cases}$$

18 where u_t is the partial derivative of u with respect to temporal variable t ; $\nabla_{\mathbf{x}} \cdot$ is a divergence
19 operator with respect to spatial variable \mathbf{x} ; $\mathbf{f}(u) = (f_1(u), \dots, f_d(u))$ is the spatial flux vector field;
20 $I = (0, T)$ is temporal interval; Γ_- is the part of the boundary $\partial\Omega \times I$ where the characteristic
21 curves enter the domain $\Omega \times I$; and the boundary data g and the initial data u_0 are given scalar-
22 valued functions.

23 Numerical methods for (1.1) have been intensively studied during the past several decades
24 by many researchers and many numerical schemes have been developed. A major difficulty in
25 simulation is that the solution of a scalar hyperbolic conservation law is often discontinuous due
26 to the discontinuous initial/boundary condition or shock formation; moreover, there is no *a priori*
27 knowledge of the location of the discontinuities. It is well-known that traditional mesh-based
28 numerical methods often exhibit oscillations near a discontinuity (called the Gibbs phenomena).
29 Such spurious oscillations are unacceptable for many applications (see, e.g., [18]). To eliminate
30 or reduce the Gibbs phenomena, finite difference and finite volume methods often use numerical
31 techniques such as limiters and filters and conservative schemes such as Roe, ENO/WENO, etc.
32 have been developed [14, 17, 18, 23]; and finite element methods usually employ discontinuous finite
33 elements [3, 8, 11] and/or adaptive mesh refinement (AMR) to generate locally refined elements
34 along discontinuous interfaces (see, e.g., [4, 19, 20]).

35 Recently, there has been increasing interests in using neural networks (NNs) to solve partial
36 differential equations (see, e.g., [1, 7, 12, 26, 30]). NNs produce a large class of functions through
37 compositions of linear transformations and activation functions. One of the striking features of
38 NNs is that this class of functions is not subject to a hand-crafted geometric mesh or point cloud

*This work was supported in part by the National Science Foundation under grant DMS-2110571.

[†]Department of Mathematics, Purdue University, 150 N. University Street, West Lafayette, IN 47907-2067
(caiz@purdue.edu, chen2042@purdue.edu).

[‡]School of Mechanical Engineering, Purdue University, 585 Purdue Mall, West Lafayette, IN 47907-
2088(liu66@purdue.edu).

as are the traditional, well-studied finite difference, finite volume, and finite element methods. The physical partition of the domain Ω , formed by free hyper-planes, can automatically adapt to the target function. To make use this powerful approximation property of NNs, in [6], we studied least-squares neural network (LSNN) method for solving linear advection-reaction problem with discontinuous solution. The LSNN method is based on a direct application of the lease-squares principle to the underlying problem studied in ([2, 9]) and on the ReLU neural network as the approximation class of functions. Compared to various AMR methods that locate the discontinuous interface through local mesh refinement, the LSNN method is much more effective in terms of the number of the degrees of freedom.

The purpose of this paper is to study the space-time LSNN method for solving the scalar hyperbolic conservation law. For the nonlinear hyperbolic conservation law, the differential equation is not generally sufficient to determine the solution. An additional constraint the so-called Rankine-Hugoniot (RH) jump condition [13, 23, 31], is needed at where the solution is not continuous. To enforce this condition weakly, [10] introduced an independent variable, the spatial-temporal flux, for the inviscid Burgers equation and applied the least-squares principle to the resulting equivalent system. A variant of this method was also studied in [10, 21] by using the Helmholtz decomposition of the flux.

Due to the training difficulty of the least-squares method of [10], in this paper we employ the naive least-squares method used for the linear advection-reaction problem [6], i.e., a direct application of least-squares principle to the PDE, initial and inflow boundary conditions. To ensure that the numerical solution enforces the RH jump condition, we introduce implicit discrete finite difference operators in section 3 by following ideas of the explicit conservative schemes such as Roe, ENO, etc.

Based on our numerical experience, it is difficult to train the network for problems with sharp changes when the LSNN method is applied to the entire computational domain Ω . This is due to the nature of nonlinear hyperbolic conservation laws since information is transported from initial and inflow boundary to the rest of the domain along the flow direction. To overcome this training difficulty, we propose the block space-time LSNN method in section 4. Basically, we partition the computational domain into a number of blocks based on the “inflow” boundary and initial conditions, then the method solves problems on these blocks sequentially. The trained parameters of the NN model for the previous block is used as an initial for the current block.

NN-based numerical methods for solving scalar nonlinear hyperbolic conservation laws have been studied recently by many researchers (see, e.g., [1, 25]). The most popular one is the so-called the physics informed neural network (PINN) method proposed in [25]. Basically, the PINN is a archaic version of the LSNN method; it employs a primitive form of least-squares formulation and uses the automatic differentiation method to differentiate the neural network. This is why the PINN and other NN-based methods are only applicable to problems with smooth solution such as the viscous Burgers equation but not the inviscid one studied in this paper.

The paper is organized as follows. The ReLU neural network and the space-time LSNN method are introduced in section 2. Conservative finite difference operators are discussed in section 3. The block LSNN method is explained in section 4. Finally, implementation and numerical results for various one dimensional benchmark test problems are presented in section 5.

2. Space-Time Least-Squares Neural Network Method. In this section, we describe least-squares neural network method for the scalar hyperbolic conservation law.

A deep neural network (DNN) defines a scalar-valued function

$$\mathcal{N} : \mathbf{z} = (\mathbf{x}, t) \in \mathbb{R}^{d+1} \longrightarrow \mathcal{N}(\mathbf{z}) \in \mathbb{R}.$$

A DNN function $\mathcal{N}(\mathbf{z})$ is typically represented as compositions of many layers of functions:

$$(2.1) \quad \mathcal{N}(\mathbf{z}) = \omega^{(L)} \left(\mathcal{N}^{(L-1)} \circ \cdots \mathcal{N}^{(2)} \circ \mathcal{N}^{(1)}(\mathbf{z}) \right) - b^{(L)},$$

87 where $\omega^{(L)} \in \mathbb{R}^{n_{L-1}}$, $b^{(L)} \in \mathbb{R}$, the symbol \circ denotes the composition of functions, and L is the
 88 depth of the network. For $l = 1, \dots, L-1$, the $\mathcal{N}^{(l)} : \mathbb{R}^{n_{l-1}} \rightarrow \mathbb{R}^{n_l}$ is called the l^{th} hidden layer
 89 of the network defined as follows:

90 (2.2)
$$\mathcal{N}^{(l)}(\mathbf{z}^{(l-1)}) = \sigma(\omega^{(l)}\mathbf{z}^{(l-1)} - \mathbf{b}^{(l)}) \quad \text{for } \mathbf{z}^{(l-1)} \in \mathbb{R}^{n_{l-1}},$$

91 where $\omega^{(l)} \in \mathbb{R}^{n_l \times n_{l-1}}$, $\mathbf{b}^{(l)} \in \mathbb{R}^{n_l}$, $\mathbf{z}^{(0)} = \mathbf{z}$, and σ is the activation function and its application to
 92 a vector is defined component-wisely. This paper will use the popular rectified linear unit (ReLU)
 93 activation function defined by

94 (2.3)
$$\sigma(s) = \max\{0, s\} = \begin{cases} 0, & \text{if } s \leq 0, \\ s, & \text{if } s > 0. \end{cases}$$

95 Denote the set of NN functions by

96
$$\mathcal{M}(\boldsymbol{\theta}, L) = \{\mathcal{N}(\mathbf{z}) = \omega^{(L)} \left(\mathcal{N}^{(L-1)} \circ \dots \circ \mathcal{N}^{(2)} \circ \mathcal{N}^{(1)}(\mathbf{z}) \right) - b^{(L)} : \omega^{(l)} \in \mathbb{R}^{n_l \times n_{l-1}}, \mathbf{b}^{(l)} \in \mathbb{R}^{n_l}\},$$

97 where $\mathcal{N}^{(l)}(\mathbf{z}^{(l-1)})$ is defined in (2.2) and $\boldsymbol{\theta}$ denotes all parameters: $\omega^{(l)}$ and $\mathbf{b}^{(l)}$ for $l = 1, \dots, L$.
 98 It is easy to see that $\mathcal{M}(\boldsymbol{\theta}, L)$ is a set, but not a linear space.

99 Applying the least-squares principle directly to the problem in (1.1), we have the following
 100 least-squares (LS) functional

101 (2.4)
$$\mathcal{L}(v; g) = \|v_t + \nabla_{\mathbf{x}} \cdot \mathbf{f}(v)\|_{0,\Omega \times I}^2 + \|v - g\|_{0,\Gamma_-}^2 + \|v(\mathbf{x}, 0) - u_0(\mathbf{x})\|_{0,\Omega}^2.$$

102 Then the least-squares approximation is to find $u_N(\mathbf{x}, t; \boldsymbol{\theta}^*) \in \mathcal{M}(\boldsymbol{\theta}, L)$ such that

103 (2.5)
$$\mathcal{L}(u_N(\cdot; \boldsymbol{\theta}^*); \mathbf{f}) = \min_{v \in \mathcal{M}(\boldsymbol{\theta}, L)} \mathcal{L}(v(\cdot; \boldsymbol{\theta}); g) = \min_{\boldsymbol{\theta} \in \mathbb{R}^N} \mathcal{L}(v(\cdot; \boldsymbol{\theta}); g),$$

104 where N is the total number of parameters in $\mathcal{M}(\boldsymbol{\theta}, L)$ given by

105
$$N = M_d(L) = \sum_{l=1}^L n_l \times (n_{l-1} + 1).$$

106 Similar to [6, 7], the integral in the LS functional is evaluated by numerical integration. To do
 107 so, let

108
$$\mathcal{T} = \{K : K \text{ is an open subdomain of } \Omega \times I\}$$

109 be a partition of the domain Ω . Then

110
$$\mathcal{E}_- = \{E = \partial K \cap \Gamma_- : K \in \mathcal{T}\} \quad \text{and} \quad \mathcal{E}_0 = \{E = \partial K \cap (\Omega \times \{0\}) : K \in \mathcal{T}\}$$

111 are partitions of the boundary Γ_- and $\Omega \times \{0\}$, respectively. Let $\mathbf{z}_K = (\mathbf{x}_K, t_K)$ and $\mathbf{z}_E = (\mathbf{x}_E, t_E)$
 112 be the centroids of $K \in \mathcal{T}$ and E in \mathcal{E}_- or \mathcal{E}_0 , respectively. Define the discrete LS functional as
 113 follows:

(2.6)
 114
$$\mathcal{L}_{\mathcal{T}}(v(\cdot; \boldsymbol{\theta}); g) = \sum_{K \in \mathcal{T}} (\delta_{\tau} v + \nabla_{\mathbf{h}} \cdot \mathbf{f}(v))^2(\mathbf{z}_K; \boldsymbol{\theta}) |K| + \sum_{E \in \mathcal{E}_-} (v - g)^2(\mathbf{z}_E; \boldsymbol{\theta}) |E| + \sum_{E \in \mathcal{E}_0} (v - u_0)^2(\mathbf{z}_E; \boldsymbol{\theta}) |E|,$$

115 where $|K|$ and $|E|$ are the d and $d-1$ dimensional measures of K and E , respectively; δ_{τ} and
 116 $\nabla_{\mathbf{h}}$ are finite difference operators to be defined in the subsequent section. Then the discrete
 117 least-squares approximation is to find $u_{\mathcal{T}}(\mathbf{z}, \boldsymbol{\theta}^*) \in \mathcal{M}(\boldsymbol{\theta}, L)$ such that

118 (2.7)
$$\mathcal{L}_{\mathcal{T}}(u_{\mathcal{T}}(\cdot; \boldsymbol{\theta}^*); g) = \min_{v \in \mathcal{M}(\boldsymbol{\theta}, L)} \mathcal{L}_{\mathcal{T}}(v(\cdot; \boldsymbol{\theta}); g) = \min_{\boldsymbol{\theta} \in \mathbb{R}^N} \mathcal{L}_{\mathcal{T}}(v(\cdot; \boldsymbol{\theta}); g).$$

119 **3. Conservative Finite Volume Operator.** How to discretize the differential operator is
 120 critical for the success of the LSNN method. Using finite difference quotient along coordinate
 121 directions to approximate the differential operator usually results in very poor numerical approxi-
 122 mation. To overcome this difficulty, we employ conservative finite volume schemes to evaluate the
 123 derivatives in the least-squares functional in (2.6). There are many conservative schemes such as
 124 Roe's scheme, ENO, and WENO, etc. (see, e.g., [27, 28, 29]). For simplicity, we briefly describe
 125 the finite volume operator using the idea of either Roe's scheme or second-order accurate ENO in
 126 this section. Note that the finite volume operators described in this section is implicit in time.

127 For any $K \in \mathcal{T}$, let (\mathbf{x}_K, t_K) be the centroid of K . Let $(\mathbf{h}, \tau) = (h_1, \dots, h_d, \tau)$ be a step size
 128 such that $(\mathbf{x}_K \pm \mathbf{h}/2, t_K \pm \tau/2) \in K$. For $i = 1, \dots, d$, let $\mathbf{h}_i = h_i \mathbf{e}_i$, where \mathbf{e}_i is the unit vector
 129 in the x_i -coordinate direction. Then the finite volume operator of the least-squares functional in
 130 (2.6) at the point (\mathbf{x}_K, t_K) is given by

$$131 \quad (\delta_\tau v + \nabla_{\mathbf{h}} \cdot \mathbf{f}(v))(\mathbf{x}_K, t_K) \\ 132 \quad (3.1) \quad = \frac{v(\mathbf{x}_K, t_K) - v(\mathbf{x}_K, t_K - \frac{1}{2}\tau)}{\tau} + \sum_{i=1}^d \frac{\hat{f}_i(v(\mathbf{x}_K + \frac{1}{2}\mathbf{h}_i, t_K)) - \hat{f}_i(v(\mathbf{x}_K - \frac{1}{2}\mathbf{h}_i, t_K))}{h_i},$$

133 where $\hat{f}_i(v(\mathbf{x}_K \pm \frac{1}{2}\mathbf{h}_i, t_K))$ are the i^{th} component of the numerical flux at $(\mathbf{x}_K \pm \frac{1}{2}\mathbf{h}_i, t_K)$. Various
 134 conservative schemes are more or less on how to reconstruct proper numerical flux.

135 Below, we describe the numerical fluxes by Roe and ENO. To this end, we introduce the Roe
 136 speed at point $(\mathbf{x}_K \pm \frac{1}{2}\mathbf{h}_i, t_K)$ in the \mathbf{e}_i direction

$$137 \quad (3.2) \quad a_i \left(\mathbf{x}_K \pm \frac{1}{2}\mathbf{h}_i, t_K \right) = \begin{cases} \frac{f_i(v(\mathbf{x}_K \pm \mathbf{h}_i, t_K)) - f_i(v(\mathbf{x}_K, t_K))}{v(\mathbf{x}_K \pm \mathbf{h}_i, t_K) - v(\mathbf{x}_K, t_K)}, & \text{if } v(\mathbf{x}_K \pm \mathbf{h}_i, t_K) \neq v(\mathbf{x}_K, t_K), \\ f'_i(v(\mathbf{x}_K, t_K)), & \text{if } v(\mathbf{x}_K \pm \mathbf{h}_i, t_K) = v(\mathbf{x}_K, t_K). \end{cases}$$

138 Then the i^{th} components of the Roe numerical flux at $(\mathbf{x}_K \pm \frac{1}{2}\mathbf{h}_i, t_K)$ are given by

$$139 \quad \hat{f}_i \left(v(\mathbf{x}_K \pm \frac{1}{2}\mathbf{h}_i, t_K) \right) \\ 140 \quad (3.3) \quad = \frac{f_i(v(\mathbf{x}_K, t_K)) + f_i(v(\mathbf{x}_K \pm \mathbf{h}_i, t_K))}{2} \mp \left| a_i \left(\mathbf{x}_K \pm \frac{1}{2}\mathbf{h}_i, t_K \right) \right| \frac{v(\mathbf{x}_K \pm \mathbf{h}_i, t_K) - v(\mathbf{x}_K, t_K)}{2}.$$

141 The key idea of the Roe's scheme is to use only grid points, if possible, on one side of the
 142 interface for constructing a finite volume scheme so that the RH condition is not violate. This is
 143 done through the signs of the Roe speed a_i at midpoints. This key idea was further explored for
 144 developing higher order schemes, e.g., the ENO schemes introduced in [16] (see also [28, 29]), by
 145 employing extra grid points. To make sure all used grid points locate on one side of the interface,
 146 it requires additional decisions and, hence, the ENO schemes are generally sophisticated.

147 For simplicity, we describe the second order ENO numerical flux here. The ENO uses the sign
 148 of the Roe speed to build up upwind scheme. Specifically,

$$149 \quad (3.4) \quad \hat{f}_i \left(v(\mathbf{x}_K + \frac{1}{2}\mathbf{h}_i, t_K) \right) = \begin{cases} \hat{f}_i^-(v(\mathbf{x}_K + \frac{1}{2}\mathbf{h}_i, t_K)), & \text{if } a_i(\mathbf{x}_K + \frac{1}{2}\mathbf{h}_i, t_K) \geq 0, \\ \hat{f}_i^+(v(\mathbf{x}_K + \frac{1}{2}\mathbf{h}_i, t_K)), & \text{if } a_i(\mathbf{x}_K + \frac{1}{2}\mathbf{h}_i, t_K) < 0. \end{cases}$$

150 Additionally, the ENO uses the magnitudes of the finite difference quotient of the i^{th} com-
 151 ponent of the flux with respect to x_i over the neighbouring intervals to determine which side of grid

152 points are used. In this way, the ENO again tries to use grid points on one side of the discontinuity
 153 if possible. More precisely, let

$$154 \quad f_i(\mathbf{x}_K, t_K; \mathbf{h}_i) := \frac{f_i(v(\mathbf{x}_K + \frac{1}{2}\mathbf{h}_i, t_K)) - f_i(v(\mathbf{x}_K, t_K))}{h_i}$$

$$155 \quad \text{and } f_i(\mathbf{x}_K, t_K; -\mathbf{h}_i) := \frac{f_i(v(\mathbf{x}_K, t_K)) - f_i(v(\mathbf{x}_K - \frac{1}{2}\mathbf{h}_i, t_K))}{h_i}.$$

156 In the case that $a_i(\mathbf{x}_K + \frac{1}{2}\mathbf{h}_i, t_K) \geq 0$, combining with (3.4), the ENO numerical flux is given by

$$157 \quad \hat{f}_i^-(v(\mathbf{x}_K + \frac{1}{2}\mathbf{h}_i, t_K)) \\ 158 \quad (3.5) \quad = \begin{cases} -\frac{1}{2}f_i(v(\mathbf{x}_K - \mathbf{h}_i, t_K)) + \frac{3}{2}f_i(v(\mathbf{x}_K, t_K)), & \text{if } |f_i(\mathbf{x}_K, t_K; -\mathbf{h}_i)| < |f_i(\mathbf{x}_K, t_K; \mathbf{h}_i)|, \\ \frac{1}{2}f_i(v(\mathbf{x}_K, t_K)) + \frac{1}{2}f_i(v(\mathbf{x}_K + \mathbf{h}_i, t_K)), & \text{if } |f_i(\mathbf{x}_K, t_K; -\mathbf{h}_i)| \geq |f_i(\mathbf{x}_K, t_K; \mathbf{h}_i)|. \end{cases}$$

159 If $a_i(\mathbf{x}_K + \frac{1}{2}\mathbf{h}_i, t_K) < 0$, then the numerical flux is reconstructed by

$$160 \quad \hat{f}_i^+(v(\mathbf{x}_K + \frac{1}{2}\mathbf{h}_i, t_K)) \\ 161 \quad = \begin{cases} \frac{1}{2}f_i(v(\mathbf{x}_K, t_K)) + \frac{1}{2}f_i(v(\mathbf{x}_K + \mathbf{h}_i, t_K)), & \text{if } |f_i(\mathbf{x}_K + \mathbf{h}_i, t_K; -\mathbf{h}_i)| < |f_i(\mathbf{x}_K + \mathbf{h}_i, t_K; \mathbf{h}_i)|, \\ \frac{3}{2}f_i(v(\mathbf{x}_K + \mathbf{h}_i, t_K)) - \frac{1}{2}f_i(v(\mathbf{x}_K + 2\mathbf{h}_i, t_K)), & \text{if } |f_i(\mathbf{x}_K + \mathbf{h}_i, t_K; -\mathbf{h}_i)| \geq |f_i(\mathbf{x}_K + \mathbf{h}_i, t_K; \mathbf{h}_i)|. \end{cases}$$

162 In a similar fashion, $\hat{f}_i(v(\mathbf{x}_K - \frac{1}{2}\mathbf{h}_i, t_K))$ may be defined accordingly.

163 **4. Block Space-Time Least-Squares Neural Network Method.** Our numerical results
 164 show that it is difficult to train the space-time LSNN method for problems with shock formation
 165 when the computational domain Ω is relatively large, even though the NN model we used is
 166 relatively small for approximating the solution of the underlying problem well. This is due to the
 167 nature of nonlinear hyperbolic conservation laws since information is transported from initial and
 168 inflow boundary to the rest of the domain along the flow direction. To overcome this training
 169 difficulty, we propose the block space-time LSNN method.

170 For clarity of exposition, let us consider one-dimensional problem defined on $\Omega = (a, b) \times (0, T)$.
 171 Without loss of generality, assume that $\tilde{\Gamma}_- = \{(a, t) | t \in (0, T)\}$ is the part of the boundary where
 172 the characteristic curves enter the domain Ω . Hence,

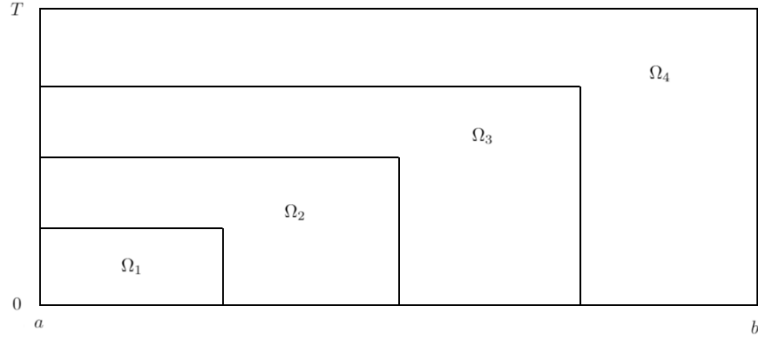
$$173 \quad \Gamma_- = \tilde{\Gamma}_- \cup \{(x, 0) | x \in (0, T)\}$$

174 is the “inflow” boundary of Ω . Let m_0 be a positive integer and let

$$175 \quad \Omega_1 = \left(a, a + \frac{b-a}{m_0}\right) \times \left(0, \frac{T}{m_0}\right) \quad \text{and } \Omega_i = \left(a, a + i\frac{b-a}{m_0}\right) \times \left(0, i\frac{T}{m_0}\right) \setminus \Omega_{i-1}$$

176 for $i = 2, \dots, m_0$. The sketch of domains $\{\Omega_i\}_{i=1}^{m_0}$ is presented in Fig 1 and it is clear that $\{\Omega_i\}_{i=1}^{m_0}$
 177 forms a partition of the domain Ω . Denote by $u_i = u|_{\Omega_i}$ the restriction of the solution u of (1.1)
 178 on Ω_i , then u_i is the solution of the following problem:

$$179 \quad (4.1) \quad \begin{cases} (u_i)_t + \nabla_{\mathbf{x}} \cdot \mathbf{f}(u_i) = 0, & \text{in } \Omega_i \in \mathbb{R}^2, \\ u_i = g, & \text{on } \Gamma_-^i = \Gamma_- \cap \partial\Omega_i, \\ u_i = u_{i-1}, & \text{on } \Gamma_{i-1,i} = \partial\Omega_{i-1} \cap \partial\Omega_i \end{cases}$$

FIG. 1. *Sketch of domains $\{\Omega_i\}_{i=1}^{m_0}$ for $m_0 = 4$* 180 for $i = 1, \dots, m_0$, where $\partial\Omega_0 = \emptyset$.

181 Define the least-squares functional for problem (4.1) by

182
$$\mathcal{L}^i(v; u_{i-1}, g) = \|v_t(\mathbf{x}, t) + \nabla_{\mathbf{x}} \cdot \mathbf{f}(v)\|_{0, \Omega_i}^2 + \|v - g\|_{0, \Gamma_-^i}^2 + \|v - u_{i-1}\|_{0, \Gamma_{i-1, i}}^2.$$

183 Then the corresponding discrete least-squares functional $\mathcal{L}_\tau^i(v(\cdot; \boldsymbol{\theta}); u_{i-1}, g)$ over the subdomain
184 Ω_i may be defined in a similar fashion as in (2.6). Now, the block space-time LSNN method is to
185 find $u_\tau^i(\mathbf{z}, \boldsymbol{\theta}_i^*) \in \mathcal{M}(\boldsymbol{\theta}, L)$ such that

186 (4.2)
$$\mathcal{L}_\tau^i(u_\tau^i(\cdot; \boldsymbol{\theta}_i^*); u_{i-1}, g) = \min_{v \in \mathcal{M}(\boldsymbol{\theta}, L)} \mathcal{L}_\tau^i(v(\cdot; \boldsymbol{\theta}); u_{i-1}, g) = \min_{\boldsymbol{\theta} \in \mathbb{R}^N} \mathcal{L}_\tau^i(v(\cdot; \boldsymbol{\theta}); u_{i-1}, g)$$

187 for $i = 1, \dots, m_0$.188 REMARK 4.1. *The NN model $\mathcal{M}(\boldsymbol{\theta}, L)$ is determined by the first subdomain and will be used for
189 all subdomains. The trained parameter $\boldsymbol{\theta}_i^*$ from the i^{th} -subdomain is a good approximation to the
190 parameters of the $(i+1)^{th}$ -subdomain and, hence, may be used as an initial. This is because the
191 solution in the current block is the evolution of the solution in the previous block.*192 The block space-time LSNN method is based on a proper partition of the domain Ω depending
193 on the “inflow” boundary of the domain. For example, in one dimension again, if

194
$$\Gamma_- = \{(x, t) \in [a, b] \times [0, T] \mid x = a, x = b, \text{ or } t = 0\},$$

195 then the domain Ω may be partitioned by time blocks as

196 (4.3)
$$\Omega_i = (a, b) \times ((i-1)T/m_0, iT/m_0)$$

197 for $i = 1, \dots, m_0$. Then the block space-time LSNN method may be defined accordingly.198 **5. Implementation and Numerical Experiments.** In this section, we present numerical
199 results for one dimensional benchmark test problems. Test problems include scalar nonlinear
200 hyperbolic conservation law: (1) inviscid Burgers equation, i.e., $\mathbf{f}(u) = \frac{1}{2}u^2$ (section 5.1-5.2) and
201 (2) $\mathbf{f}(u) = \frac{1}{4}u^4$ (section 5.3). Additionally, we analyze the effects of integration mesh and network
202 structure in section 5.4; and compare the Roe and ENO schemes in section 5.5.203 The domain $\Omega = (a, b) \times (0, T)$ is partitioned into time blocks as (4.3) and m_0 is the number of
204 blocks. Unless otherwise stated, the integration mesh \mathcal{T} is obtained by uniformly partitioning all
205 subdomains Ω_i into identical squares with the mesh size $h = 0.01$ for $i = 1, \dots, m_0$. To preserve
206 the conservation, the spatial mesh size h_i and the temporal step size τ in both Roe (3.1) and ENO
207 (3.5) schemes are chosen to be the same as the integration mesh size, i.e., $h_i = \tau = h = 0.01$.

208 The block space-time LSNN method is implemented, and the minimization problem in (4.2) is
 209 numerically solved using the Adams version of gradient descent [22] with a fixed or an adaptive
 210 learning rate.

211 As shown in [6], a three-layer NN is needed in order to approximate discontinuous solutions
 212 along non-straight line interfaces. Since there is no prior knowledge of geometric shape of the
 213 discontinuous interfaces for nonlinear problems, we use three-layer NN models for all test problems.
 214 Moreover, the same architecture of three-layer NN models are used for all blocks. As suggested
 215 in Remark 4.1, the parameters of the NN for the current block are initialized by the values of the
 216 parameters of the NN in the previous block. For the first block, the parameters of the second
 217 hidden layer are initialized randomly; and those of the first hidden layer are initialized using the
 218 strategy introduced in [?]. For convenience of readers, we briefly describe here. Let $\omega_i \in \mathcal{S}^1$ and
 219 $b_i \in \mathbb{R}$ be the weights and bias of the i^{th} neuron of the first hidden layer of the first block NN
 220 model, respectively, where \mathcal{S}^1 is the unit circle in \mathbb{R}^2 . Initial of $\{(\omega_i, b_i)\}_{i=1}^{n_1}$ is chosen so that
 221 the hyper-planes $\{\omega_i \cdot (x, t) = b_i\}_{i=1}^{n_1}$ form a uniform partition of the first block Ω_1 . In addition,
 222 without an effective training strategy, we observe from the experiment that adding a weight α to
 223 the L^2 loss of the initial condition is helpful for the training. Specifically, the following least-squares
 224 functional is used in the implementation

$$225 \quad (5.1) \quad \mathcal{L}^i(v; u_{i-1}, g) = \|v_t(x, t) + \nabla_x \mathbf{f}(v)\|_{0, \Omega_i}^2 + \|v - g\|_{0, \Gamma_{i-1, i}}^2 + \alpha \|v - u_{i-1}\|_{0, \Gamma_{i-1, i}}^2 \quad \text{for } i = 1, \dots, m_0$$

226 and the weight α is empirically determined.

227 Let u_i be the solution of the problem in (4.1) and $u_{i,\tau}$ be the NN approximation. **Using all**
 228 **quadrature points including those near the discontinuity**, the relative error in the L^2 norm for
 229 each block is reported in Table 1-8. Note that the **points near discontinuity are usually excluded**
 230 **when reporting the error of existing traditional methods**. The network structure is expressed as
 231 $2-n_1-n_2-1$ for a three-layer network with n_1 and n_2 neurons in the respective first and second
 232 layers. The traces of the exact solution and the numerical approximation are depicted in Figures
 233 2-7 on a plane perpendicular to the space-time plane. Those traces exhibit the capability of the
 234 numerical approximation in resolving the shock/rarefaction. Since those planes are generally not
 235 perpendicular to the discontinuous interface, the errors shown in those traces are larger than the
 236 actual error.

237 **5.1. Riemann problem for the inviscid Burgers equation.** For the one dimensional
 238 inviscid Burgers equation, $\mathbf{f}(u) = f(u) = \frac{1}{2}u^2$, we report numerical results for the corresponding
 239 Riemann problem where the initial condition with a single discontinuity is given by:

$$240 \quad (5.2) \quad u_0(x) = \begin{cases} u_L, & \text{if } x \leq 0, \\ u_R, & \text{if } x > 0. \end{cases}$$

241 When $u_L > u_R$, the characteristic lines intersect and a shock forms immediately for $t > 0$. The
 242 weak solution is given by

$$243 \quad (5.3) \quad u(x, t) = \begin{cases} u_L, & \text{if } x \leq st, \\ u_R, & \text{if } x > st, \end{cases}$$

244 with the shock speed determined by the RH condition

$$245 \quad s = \frac{f(u_L) - f(u_R)}{u_L - u_R}.$$

246 When $u_L < u_R$, the range of influence of all points in \mathbb{R} is a proper subset of $\mathbb{R} \times [0, \infty)$. This
 247 fact implies that the weak solution of the scalar hyperbolic conservation law is not unique. To

248 ensure the underlying Cauchy problem having a unique solution over the whole domain $\mathbb{R} \times [0, \infty)$,
 249 the so-called vanishing viscosity weak solution is introduced (see, e.g., [13, 23, 31]) and given by

$$250 \quad u(x, t) = \begin{cases} u_L, & \text{if } x < u_L t, \\ x/t, & \text{if } u_L t \leq x \leq u_R t, \\ u_R, & \text{if } x > u_R t. \end{cases}$$

251 **5.1.1. Shock formation.** The first test problem is corresponding to the case

$$252 \quad u_L = 1 > 0 = u_R$$

253 with a computational domain $\Omega = (-1, 2) \times (0, 1)$. The inflow boundary is

$$254 \quad \Gamma_- = \Gamma_-^L \cup \Gamma_-^R \equiv \{(-1, t) : t \in [0, 1]\} \cup \{(2, t) : t \in [0, 1]\}$$

255 with the boundary conditions: $g = u_L$ on Γ_-^L and $g = u_R$ on Γ_-^R . The block space-time LSNN
 256 method is employed with $m_0 = 5$ blocks, a fixed learning rate 0.003, and 30000 iterations for each
 257 block.

258 The set of experiments is done by using the numerical fluxes of Roe (3.1) and the second
 259 order ENO (3.5). By choosing $\alpha = 20$ in (5.1), numerical results of both schemes are reported
 260 in Table 1. Since the results of the Roe flux are similar, Figure 2 (b)-(f) only depict the traces
 261 of the exact and numerical solution generated by the ENO flux on the planes $t = iT/m_0$ for
 262 $i = 1, \dots, m_0$. Clearly, the block space-time LSNN method with a conservative scheme is able to
 263 resolve the shock and accurately approximate the solution without the Gibbs phenomena. For this
 264 simple Riemann problem, Roe and ENO schemes produce similar results. Given the additional
 265 evaluations involving in the ENO scheme, we do not observe many advantages of using higher-order
 266 scheme for flux reconstruction despite the fact that ENO performs slightly better in the L^2 relative
 267 errors.

TABLE 1
Relative errors of Riemann problem (shock) for Burgers' equation using Roe and ENO fluxes

Network structure	Block	Roe flux $\frac{\ u_i - u_{i,\tau}\ _0}{\ u_i\ _0}$	ENO flux $\frac{\ u_i - u_{i,\tau}\ _0}{\ u_i\ _0}$
2-10-10-1	Ω_1	0.049553	0.030901
2-10-10-1	Ω_2	0.046321	0.030178
2-10-10-1	Ω_3	0.044123	0.028984
2-10-10-1	Ω_4	0.042621	0.028791
2-10-10-1	Ω_5	0.041182	0.032253

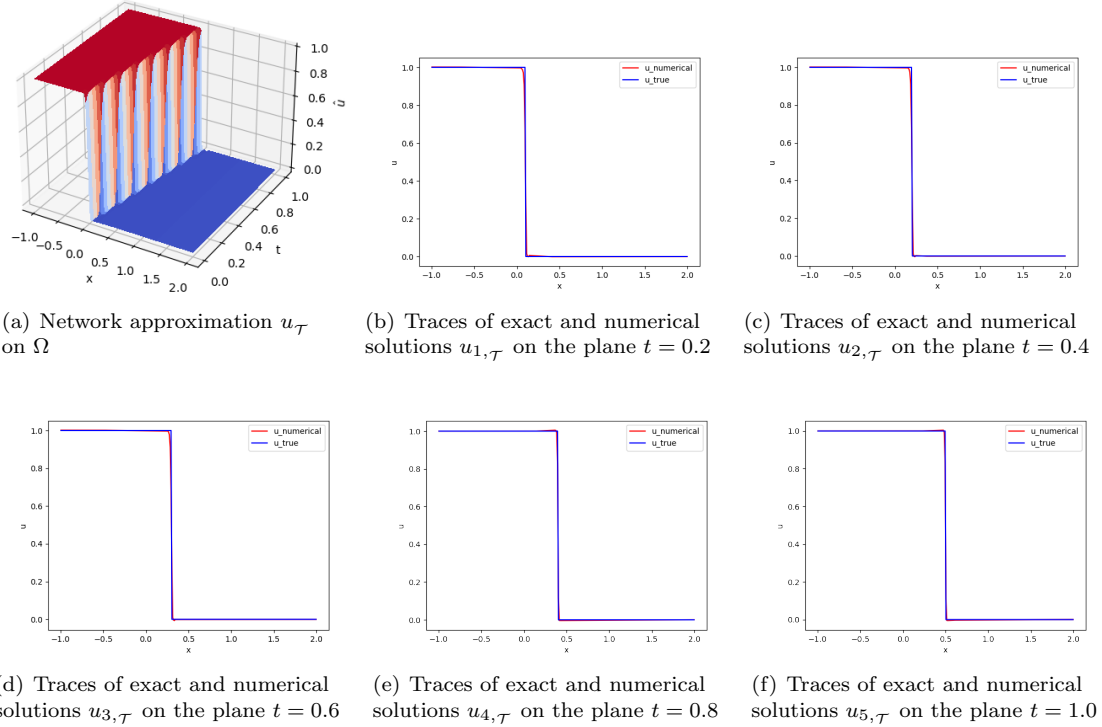
268 **5.1.2. Rarefaction waves.** The second test problem is corresponding to the case

$$269 \quad u_L = 0 < 1 = u_R$$

270 with a computational domain $\Omega = (-1, 2) \times (0, 0.2)$. The inflow boundary is

$$271 \quad \Gamma_- = \Gamma_-^L \cup \Gamma_-^R \equiv \{(-1, t) : t \in [0, 0.2]\} \cup \{(2, t) : t \in [0, 0.2]\}$$

272 with the boundary conditions: $g = u_L$ on Γ_-^L and $g = u_R$ on Γ_-^R . The block space-time LSNN
 273 method is employed with $m_0 = 2$ blocks, a fixed learning rate 0.003, and 20000 iterations for each
 274 block.

FIG. 2. *Approximation results of Riemann problem (shock) for Burgers' equation using Roe flux*

275 Numerical results of a 2-10-10-1 network using the Roe flux (3.1) are reported in Table 2. The
 276 traces of the exact and numerical solutions in Fig. 3 indicate that Roe's scheme fails to resolve the
 277 rarefaction. For the traditional mesh-based method, it is well-known that Roe's scheme is not able
 278 to compute the physical solution of the rarefaction wave. This is because the scheme approximates
 279 the numerical flux depending the sign of the speed a_i (3.2) at midpoints. If the sign differs on two
 280 sides and $u(x, t)$ travels slower on the left, Roe's scheme may not be able to capture such behavior.
 281 From this perspective, we observe certain limitations of using such conservative scheme and that
 282 the discretization scheme is very important for the block space-time LSNN method.

283 REMARK 5.1. In [15, 23], the authors proposed the “entropy fix” traditional mesh-based ap-
 284 proach to address such issue. In a forthcoming paper, we will propose a discretization scheme for
 285 the LSNN method which is capable of resolving the rarefaction.

TABLE 2
Relative errors of Riemann problem (rarefaction) for Burgers' equation using Roe flux

Network structure	Time block	$\frac{\ u_i - u_{i,\tau}\ _0}{\ u_i\ _0}$
2-10-10-1	Ω_1	0.047435
2-10-10-1	Ω_2	0.074521

286 **5.2. Inviscid Burgers equation with smooth initial condition.** The third problem is
 287 again the Burgers equation defined on the computational domain $\Omega = (0, 2) \times (0, 0.4)$ with the

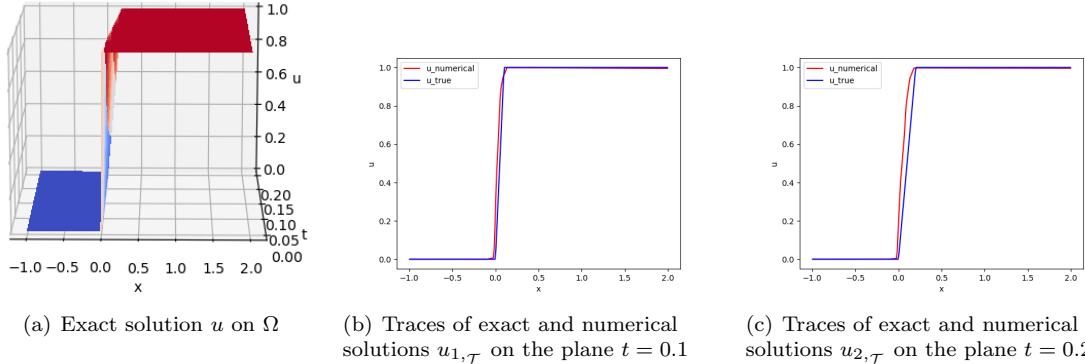


FIG. 3. Approximation results of Riemann problem (rarefaction) for Burgers' equation using Roe flux

288 inflow boundary

$$289 \quad \Gamma_- = \Gamma_-^L \cup \Gamma_-^R \equiv \{(0, t) : t \in [0, 0.4]\} \cup \{(2, t) : t \in [0, 0.4]\}$$

290 and a sinusoidal initial condition

$$291 \quad u_0(x) = 0.5 + \sin(\pi x).$$

292 The shock forms at $t = 1/\pi \approx 0.318$. Since the exact solution of the test problem is defined
293 implicitly, in order to measure the quality of the NN approximation, we generate a benchmark
294 reference solution \hat{u} using the traditional mesh-based approach. Specifically, the third order ac-
295 curate WENO scheme [28] is employed for the spatial discretization with a fine grid ($\Delta x = 0.001$
296 and $\Delta t = 0.0002$) on the computational domain Ω ; and the fourth order Runge-Kutta method is
297 used for the temporal discretization [32]. The block space-time LSNN method is implemented with
298 $m_0 = 8$ blocks and an adaptive learning rate which starts at 0.005 and decays by half for every
299 25000 iterations. The learning rate decay strategy is employed with 50000 iterations on each time
300 block.

301 Since the initial condition of the test problem is a smooth function, it is expected that a
302 network with additional neurons is needed for approximation. Choosing $\alpha = 5$ in (5.1), the
303 numerical results of a 2-30-30-1 network using the ENO flux in (3.5) are reported in Table 3.
304 Figure 4 depicts the traces of the reference solution and numerical approximation on the plane
305 $t = iT/m_0$ for $i = 1, \dots, m_0$. We observe some error accumulation when block evolves, and the
306 block space-time LSNN method can resolve the shock. It is noticeable in Fig. 4 that approximation
307 near the local maximum is poor. Possibly this is due to inaccuracy of the second order ENO scheme
308 for complicated initial data. A new and accurate discretization scheme for the LSNN method will
309 be reported in a forthcoming paper [5].

310 **5.3. Riemann problem with $f(u) = \frac{1}{4}u^4$.** The fourth numerical experiment is the Riemann
311 shock problem with a convex flux $\mathbf{f}(u) = f(u) = \frac{1}{4}u^4$. We choose the initial condition

$$312 \quad u_L = 1 > 0 = u_R$$

313 in (5.2), then the weak solution is given by (5.3) with the speed $s = 1/4$. The computational
314 domain of problem is given by $\Sigma = (-1, 1) \times (0, 1)$ and the inflow boundary is

$$315 \quad \Gamma_- = \Gamma_-^L \cup \Gamma_-^R \equiv \{(-1, t) : t \in [0, 1]\} \cup \{(1, t) : t \in [0, 1]\}$$

316 with the boundary conditions: $g = 1$ on Γ_-^L and $g = 0$ on Γ_-^R .

TABLE 3
Relative errors of Burgers' equation with a sinusoidal initial condition using ENO flux

Network structure	Time block	$\frac{\ \hat{u}_i - u_{i,\tau}\ _0}{\ \hat{u}_i\ _0}$
2-30-30-1	Ω_1	0.010461
2-30-30-1	Ω_2	0.012517
2-30-30-1	Ω_3	0.019772
2-30-30-1	Ω_4	0.022574
2-30-30-1	Ω_5	0.029011
2-30-30-1	Ω_6	0.038852
2-30-30-1	Ω_7	0.075888
2-30-30-1	Ω_8	0.078581

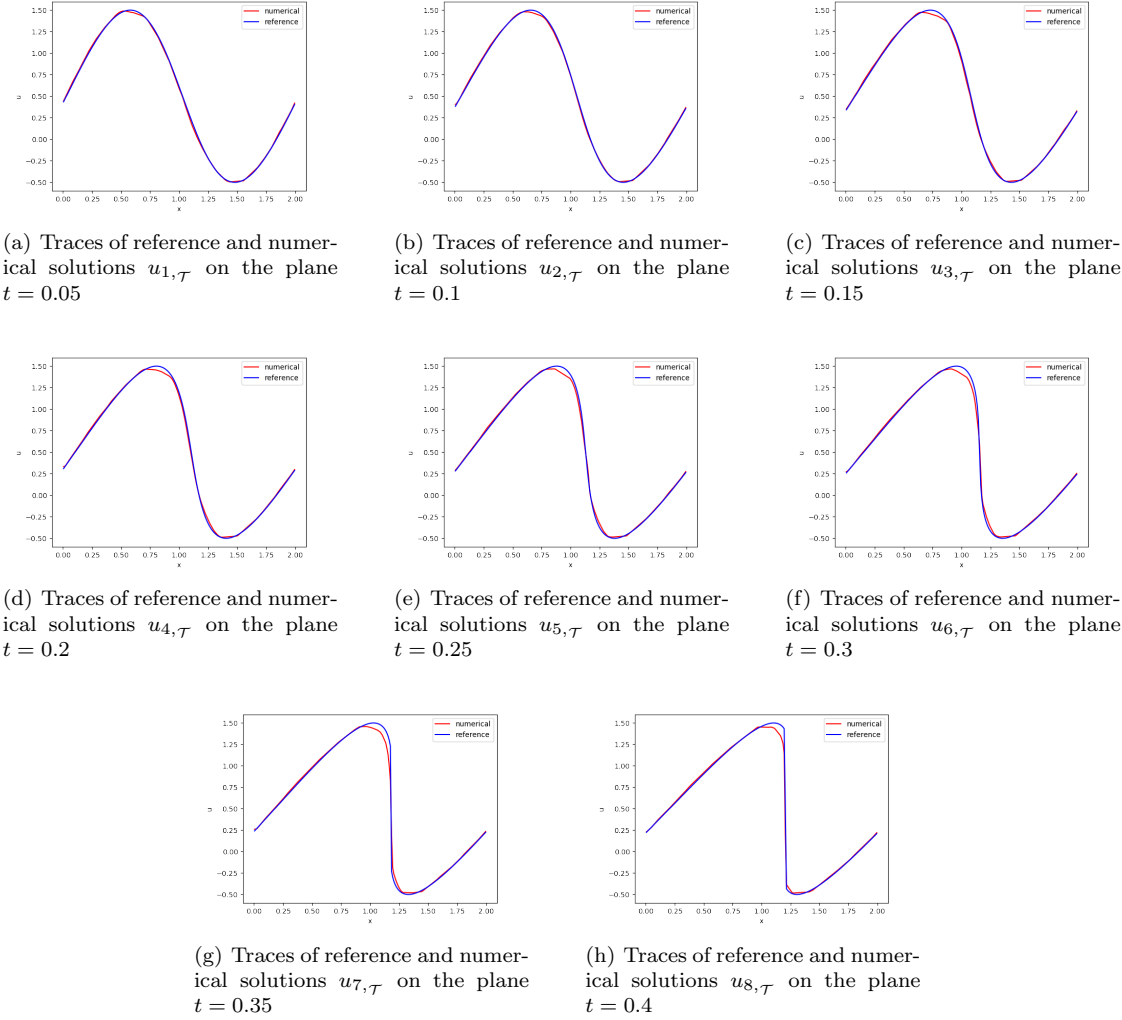


FIG. 4. *Approximation results of Burgers' equation with a sinusoidal initial using ENO flux*

317 Empirically, we choose $\alpha = 20$ in (5.1) in the implementation. Employing the block space-time
 318 LSNN method with $m_0 = 5$ blocks, a fixed learning rate 0.003 and 30000 iterations for each block,
 319 we report the numerical results of a 2-10-10-1 network in Table 4 and Fig. 5. Obviously, the
 320 discontinuous interface can be accurately captured as the NN approximation is almost overlapped
 321 with the exact solution, which suggests that the LSNN method is not only capable of solving the
 Burgers equation but also the problem with a general convex flux.

TABLE 4
Relative errors of Riemann problem (shock) with $f(u) = \frac{1}{4}u^4$ using Roe flux

Network structure	Block	$\frac{\ u_i - u_{i,\tau}\ _0}{\ u_i\ _0}$
2-10-10-1	Ω_1	0.035034
2-10-10-1	Ω_2	0.036645
2-10-10-1	Ω_3	0.036798
2-10-10-1	Ω_4	0.037217
2-10-10-1	Ω_5	0.037451

322

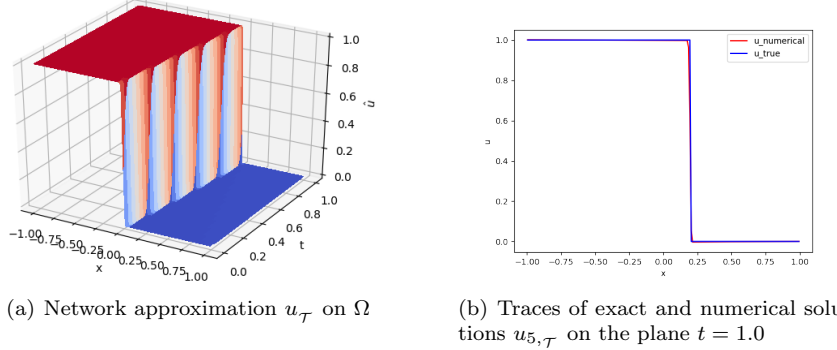


FIG. 5. *Approximation results of Riemann problem (shock) with $f(u) = \frac{1}{4}u^4$ using Roe flux*

323 **5.4. Effects of integration mesh and network structure.** The goal of this section is to
 324 analyze the effects of integration mesh and network structure for the LSNN method. Specifically,
 325 we use the inviscid Burgers equation defined on the computational domain $\Omega = (-1, 2) \times (0, 0.6)$
 326 with a continuous piece-wise linear initial condition

$$327 \quad u_0(x) = \begin{cases} 1, & \text{if } x < 0, \\ 1 - 2x, & \text{if } 0 \leq x \leq 1/2, \\ 0, & \text{if } x > 1/2. \end{cases}$$

328 The inflow boundary is

$$329 \quad \Gamma_- = \Gamma_-^L \cup \Gamma_-^R \equiv \{(-1, t) : t \in [0, 0.6]\} \cup \{(2, t) : t \in [0, 0.6]\},$$

330 with the boundary conditions: $g = 1$ on Γ_-^L and $g = 0$ on Γ_-^R . Even though the initial value
 331 u_0 is continuous, the shock will appear at some point since $u(x, t)$ travels faster on the left-hand
 332 side than on the right-hand side. Specifically, when $t < 1/2$, the solution is continuous and it is

333 determined by the characteristic lines as well as the initial conditions:

$$334 \quad u(x, t) = \begin{cases} 1, & \text{if } x < t < 1/2, \\ \frac{1-2x}{1-2t}, & \text{if } t \leq x \leq 1/2, \\ 0, & \text{if } x > 1/2. \end{cases}$$

335 When $t > 1/2$, the shock forms and the desired weak solution satisfying RH condition is given by

$$336 \quad u(x, t) = \begin{cases} 1, & \text{if } x < (2t+1)/4, \\ 0, & \text{if } x \geq (2t+1)/4. \end{cases}$$

337 The block space-time LSNN is implemented with $m_0 = 3$ blocks, a fixed learning rate 0.003
 338 and $\alpha = 10$ in the training. In order to explore the network approximation power, we do not
 339 constrain the number of iterations on each block. The stopping criteria for the gradient descent
 340 solver is set as follows: the solver stops when the loss function (5.1) decreases within 0.1% in the
 341 last 2000 iterations.

342 The first set of experiments is to observe the impact of integration mesh size when a fixed
 343 network structure 2-10-10-1 is used. Starting with the same initialization for both layers, the
 344 relative L^2 errors of the ENO scheme on uniform meshes with different mesh size are reported in
 345 Table 5. The results display that the error decreases as the integration mesh size reduces, but the
 346 decreasing rate is small when the mesh size is sufficiently fine. This indicates that $h = 0.01$ is fine
 347 enough to accurately evaluate the discrete LS functional in (4.2) for the given 2-10-10-1 network.

TABLE 5
Relative L^2 errors of the problem with a piece-wise linear initial using different integration mesh sizes

Time block	Integration mesh size				
	$h = 0.1$	$h = 0.05$	$h = 0.025$	$h = 0.01$	$h = 0.005$
Ω_1	0.056712	0.029366	0.017376	0.013946	0.013121
Ω_2	0.079633	0.064069	0.048971	0.037891	0.036501
Ω_3	0.120129	0.115123	0.102844	0.084728	0.081209

348 The second set of numerical tests is to investigate the effect of network structure. To accurately
 349 evaluate the functional, we use a fine integration mesh with size $h = 0.005$. The approximation
 350 errors generated by four different network structures using the ENO scheme are presented in Table
 351 6. As expected, the approximation error decreases as the number of neurons in the network
 352 increases.

TABLE 6
Relative L^2 errors of the problem with a piece-wise linear initial using different network structures

Time block	Network structure			
	2-4-4-1	2-7-7-1	2-10-10-1	2-13-13-1
Ω_1	0.021699	0.017004	0.013121	0.009895
Ω_2	0.047953	0.040521	0.036501	0.028159
Ω_3	0.095649	0.088201	0.081209	0.072244

353 Tables 5 and 6 indicate that the approximation error grows significantly as the block evolves.
 354 To address this issue, a simple way is to decrease the size of each block, or equivalently, increase
 355 the number of blocks m_0 . Specifically, increasing m_0 from 3 to 6, Table 7 reports numerical results

356 of the ENO scheme using $h = 0.01$, which is better than the results in the corresponding column in
 357 Table 5. Due to the increasing computational cost when using a smaller block, in practice we need
 358 to balance the cost and the accuracy when choosing the size of the block in the block space-time
 359 LSNN method.

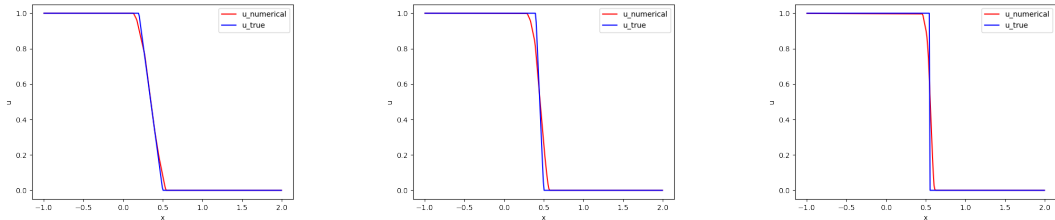
TABLE 7
Relative L^2 errors of the problem with a piece-wise linear initial using ENO flux with $m_0 = 6$

Network structure	Block	$\frac{\ u_i - u_{i,\tau}\ _0}{\ u_i\ _0}$
2-10-10-1	Ω_1	0.008958
2-10-10-1	Ω_2	0.014842
2-10-10-1	Ω_3	0.019282
2-10-10-1	Ω_4	0.025562
2-10-10-1	Ω_5	0.047431
2-10-10-1	Ω_6	0.052606

360 **5.5. Comparison of the Roe and ENO schemes.** This choosing set of numerical experiments aims to compare numerical performances of the LSNN method using the Roe (3.1) and ENO
 361 (3.5) schemes. The test problem in section 5.4 is used, and the block space-time LSNN method
 362 is employed with $m_0 = 6$ blocks, the 2-10-10-1 network structure, and with a uniform integration
 363 mesh of the size $h = 0.01$. We note that the ENO performs better than the Roe in the relative L^2
 364 norm (see Table 8) and near the discontinuous interface (see Fig. 6 and 7). Note that the former
 365 is more expansive than the latter in the computational cost due to additional testing.

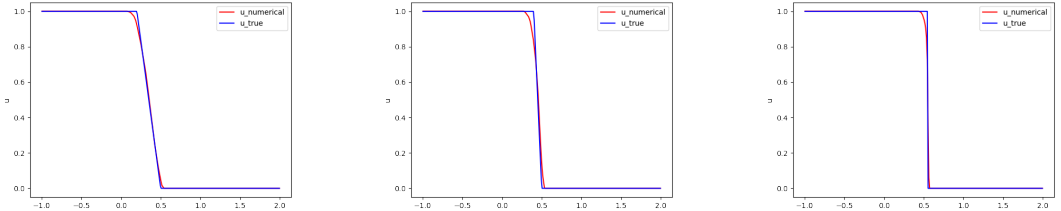
TABLE 8
Relative errors of Burgers' equation with a piece-wise linear initial condition

Network structure	Block	Roe flux $\frac{\ u_i - u_{i,\tau}\ _0}{\ u_i\ _0}$	ENO flux $\frac{\ u_i - u_{i,\tau}\ _0}{\ u_i\ _0}$
2-10-10-1	Ω_1	0.008333	0.008958
2-10-10-1	Ω_2	0.017503	0.014842
2-10-10-1	Ω_3	0.025342	0.019282
2-10-10-1	Ω_4	0.036211	0.025562
2-10-10-1	Ω_5	0.061251	0.047431
2-10-10-1	Ω_6	0.068512	0.052606



(a) Traces of exact and numerical
 solutions $u_{2,\tau}$ on the plane $t = 0.2$ (b) Traces of exact and numerical
 solutions $u_{4,\tau}$ on the plane $t = 0.4$ (c) Traces of exact and numerical
 solutions $u_{6,\tau}$ on the plane $t = 0.6$

FIG. 6. *Approximation results of Burgers' equation with a piece-wise linear initial using Roe flux*



(a) Traces of exact and numerical solutions $u_{2,\tau}$ on the plane $t = 0.2$ (b) Traces of exact and numerical solutions $u_{4,\tau}$ on the plane $t = 0.4$ (c) Traces of exact and numerical solutions $u_{6,\tau}$ on the plane $t = 0.6$

FIG. 7. *Approximation results of Burgers' equation with a piece-wise linear initial using ENO flux*

367 **6. Discussions and Conclusions.** The block space-time LSNN method is proposed for
 368 solving scalar nonlinear hyperbolic conservation laws. The least-squares formulation is a direct
 369 application of the least-squares principle to the underlying problem: the equation, the inflow
 370 boundary condition, and the initial condition. The block space-time version of the LSNN method is
 371 introduced to compensate with some uncertainty of the not well-understood nonlinear optimization
 372 procedure.

373 How to approximate the differential operator in the least-squares functional is critical for
 374 the success of the space-time LSNN method. As mentioned in the introduction, existing NN-
 375 based methods are not applicable to the inviscid Burgers equation whose solution is discontinuous.
 376 Employing the Roe and the second order ENO schemes, we show numerically that the resulting
 377 LSNN method is capable of resolving the shock without smearing and oscillations. Moreover, the
 378 LSNN method has much less degrees of freedom (DoF) than traditional mesh-based methods.

379 Despite the great potential demonstrated in this paper, the current version of the LSNN
 380 method needs to be improved in both accuracy and efficiency in order to grow into a viable
 381 numerical method. First, the method is inaccurate for complicated initial condition; moreover,
 382 it has limitations for problems with rarefaction waves and with non-convex spatial fluxes. To
 383 overcome these deficiency, we recently study a new version of the LSNN method that uses a novel
 384 and accurate finite volume method developed in [5]. Second, the computational cost of the current
 385 version of the LSNN method is expensive because of the resulting non-convex optimization. To
 386 reduce the cost, we will explore physical meanings of non-linear parameters of NNs (see, e.g., [24])
 387 to develop good initial strategies and then employ fast iterative solvers such as methods of BFGS
 388 type (the Broyden–Fletcher–Goldfarb–Shanno algorithm).

389

REFERENCES

- 390 [1] Y. Bar-Sinai, S. Hoyer, J. Hickey, and M. P. Brenner. Learning data-driven discretizations for partial differential
 391 equations. *Proceedings of the National Academy of Science of USA*, 116 (31):15344–15349, 2019.
- 392 [2] P. Bochev and J. Choi. Improved least-squares error estimates for scalar hyperbolic problems. *Computational
 393 Methods in Applied Mathematics*, 1(2):115–124, 2001.
- 394 [3] F. Brezzi, L. D. Marini, and E. Süli. Discontinuous galerkin methods for first-order hyperbolic problems.
 395 *Mathematical models and methods in applied sciences*, 14(12):1893–1903, 2004.
- 396 [4] E. Burman. A posteriori error estimation for interior penalty finite element approximations of the advection-
 397 reaction equation. *SIAM journal on numerical analysis*, 47(5):3584–3607, 2009.
- 398 [5] Z. Cai, J. Chen, and M. Liu. Finite volume least-squares neural network (FV-LSNN) method for scalar
 399 nonlinear hyperbolic conservation laws. *arXiv preprint arXiv:2110.10895*, 2021.
- 400 [6] Z. Cai, J. Chen, and M. Liu. Least-squares ReLU neural network (LSNN) method for linear advection-reaction
 401 equation. *Journal of Computational Physics*, 110514, 2021.
- 402 [7] Z. Cai, J. Chen, M. Liu, and X. Liu. Deep least-squares methods: An unsupervised learning-based numerical
 403 method for solving elliptic PDEs. *Journal of Computational Physics*, 109707, 2020.

- [8] W. Dahmen, C. Huang, C. Schwab, and G. Welper. Adaptive petrov–galerkin methods for first order transport equations. *SIAM journal on numerical analysis*, 50(5):2420–2445, 2012.
- [9] H. De Sterck, T. A. Manteuffel, S. F. McCormick, and L. Olson. Least-squares finite element methods and algebraic multigrid solvers for linear hyperbolic PDEs. *SIAM Journal on Scientific Computing*, 26(1):31–54, 2004.
- [10] H. De Sterck, T. A. Manteuffel, S. F. McCormick, and L. Olson. Numerical conservation properties of $H(\text{div})$ -conforming least-squares finite element methods for the burgers equation. *SIAM Journal on Scientific Computing*, 26(5):1573–1597, 2005.
- [11] L. Demkowicz and J. Gopalakrishnan. A class of discontinuous petrov–galerkin methods. part I: The transport equation. *Computer Methods in Applied Mechanics and Engineering*, 199(23–24):1558–1572, 2010.
- [12] W. E and B. Yu. The deep ritz method: A deep learning-based numerical algorithm for solving variational problems. *Communications in Mathematics and Statistics*, 6(1):1–12, 3 2018.
- [13] E. Godlewski and P.-A. Raviart. *Numerical approximation of hyperbolic systems of conservation laws*, volume 118. Springer Science & Business Media, 2013.
- [14] D. Gottlieb and C.-W. Shu. On the gibbs phenomenon and its resolution. *SIAM review*, 39(4):644–668, 1997.
- [15] A. Harten. High resolution schemes for hyperbolic conservation laws. *Journal of computational physics*, 135(2):260–278, 1997.
- [16] A. Harten, B. Engquist, S. Osher, and S. R. Chakravarthy. Uniformly high order accurate essentially non-oscillatory schemes, iii. In *Upwind and high-resolution schemes*, pages 218–290. Springer, 1987.
- [17] J. S. Hesthaven. *Numerical methods for conservation laws: From analysis to algorithms*. SIAM, 2017.
- [18] J. S. Hesthaven and T. Warburton. *Nodal discontinuous Galerkin methods: algorithms, analysis, and applications*. Springer Science & Business Media, 2007.
- [19] P. Houston, J. A. Mackenzie, E. Süli, and G. Warnecke. A posteriori error analysis for numerical approximations of friedrichs systems. *Numerische Mathematik*, 82(3):433–470, 1999.
- [20] P. Houston, R. Rannacher, and E. Süli. A posteriori error analysis for stabilised finite element approximations of transport problems. *Computer methods in applied mechanics and engineering*, 190(11–12):1483–1508, 2000.
- [21] D. Z. Kalchev and T. A. Manteuffel. A least-squares finite element method based on the helmholtz decomposition for hyperbolic balance laws. *arXiv preprint arXiv:1911.05831v2*, 2020.
- [22] D. P. Kingma and J. Ba. Adam: A method for stochastic optimization. In *International Conference on Representation Learning, San Diego*, 2015.
- [23] R. J. LeVeque. *Numerical methods for conservation laws*, volume 132. Springer, 1992.
- [24] M. Liu, Z. Cai, and J. Chen. Adaptive two-layer ReLU neural network: I. best least-squares approximation. *arXiv preprint arXiv:2107.08935v1*, 2021.
- [25] M. Raissi, P. Perdikaris, and G. E. Karniadakis. Physics informed deep learning (part I): Data-driven solutions of nonlinear partial differential equations. *arXiv preprint arXiv:1711.10561*, 2017.
- [26] M. Raissi, P. Perdikaris, and G. E. Karniadakis. Physics-informed neural networks: A deep learning framework for solving forward and inverse problems involving nonlinear partial differential equations. *Journal of Computational Physics*, 378:686–707, 2019.
- [27] P. L. Roe. Approximate riemann solvers, parameter vectors, and difference schemes. *Journal of computational physics*, 43(2):357–372, 1981.
- [28] C.-W. Shu. Essentially non-oscillatory and weighted essentially non-oscillatory schemes for hyperbolic conservation laws. In *Advanced numerical approximation of nonlinear hyperbolic equations*, pages 325–432. Springer, 1998.
- [29] C.-W. Shu and S. Osher. Efficient implementation of essentially non-oscillatory shock-capturing schemes. *Journal of computational physics*, 77(2):439–471, 1988.
- [30] J. Sirignano and K. Spiliopoulos. DGM: A deep learning algorithm for solving partial differential equations. *Journal of Computational Physics*, 375:1139–1364, 2018.
- [31] J. W. Thomas. *Numerical partial differential equations: finite difference methods*, volume 22. Springer Science & Business Media, 2013.
- [32] Y. Wang, Z. Shen, Z. Long, and B. Dong. Learning to discretize: solving 1D scalar conservation laws via deep reinforcement learning. *arXiv preprint arXiv:1905.11079*, 2019.